

Gauche-trans transitions in amorphous polymers under annealing: Lattice model and polarized light scattering

Masaru Matsuo,^{1,*} Yanling Luo,¹ and Andrzej Galeski²¹*Department of Apparel and Clothing Science, Faculty of Human Life and Environment, Nara Women's University, Nara 630-8506, Japan*²*Centre of Molecular and Macromolecular Studies, Polish Academy of Science, Lodz, Poland*

(Received 8 October 2008; published 10 April 2009)

The driving force of density fluctuation of amorphous polymer films under annealing processes was evaluated synthetically in terms of thermodynamics on the basis of the logarithmic light intensity as a function of annealing time. The time dependence of $\ell n(I)$ of polyethylene (terephthalate) (PET) as an example for characterizing an amorphous state was classified into three stages: the first stage (stage I), where $\ell n(I)$ showed insignificant changes with time; the second stage (stage II), where $\ell n(I)$ increased linearly; and the third stage (stage III), where the intensity deviated from the linear relationship and tended to level off. The density fluctuation by chain diffusion, termed quasi-spinodal decomposition, in stage II was analyzed in terms of an increase of trans-conformation of an amorphous chain in stage I. To provide conclusive evidence, the orientation function of chain segments was calculated by using a lattice model that accounts for entropic and energetic characters. The former character is associated with segmental orientation due to the effect of chain stiffness of Kuhn segments characterized by a rod with a relatively large length-to-width ratio x , whereas the latter is associated with thermotropic systems with anisotropic polarizabilities. By using the theoretical orientation function, Hv light scattering patterns were calculated by a statistical approach in which the optical axis of a PET chain segment was chosen along the direction perpendicular to the benzene ring. This selection was justified by comparison of the three principal refractive indexes of a PET chain. The calculated patterns provided a clear X-type lobe, when the correlation between optical elements concerning the rotational fluctuation became stronger. The calculated patterns were in good agreement with the patterns observed in stage III. The series of experimental and theoretical results indicated that the conversion from gauche- to trans-conformation plays an important role to derive the density fluctuation of amorphous polymer chains associated with the initiation of crystallization.

DOI: [10.1103/PhysRevE.79.041801](https://doi.org/10.1103/PhysRevE.79.041801)

PACS number(s): 36.20.-r, 61.41.+e, 81.10.-h

I. INTRODUCTION

There are a number of papers describing the kinetics of crystallization of polymers in terms of crystal growth and the initiation of crystallization relating to the nucleation step. This concept is due to experimental evidence that polymer crystallization may be assisted by the formation of an intermediate metastable state, and the long-range structure due to some structure relaxations is formed during the annealing processes. Among crystalline polymers, polyethylene terephthalate (PET) can form amorphous films. As such, PET provides the opportunity to study crystallization kinetics during the induction period, which is defined as the time required for the formation of high-density regions exceeding the critical size directly from the homogeneous amorphous state [1–10].

Apart from the observation of crystal growth processes, crystallization of PET has been studied primarily by depolarized light scattering under the induction period in terms of density fluctuation of the amorphous phase [1,8,9]. The results show that the period is associated with spinodal decomposition (SD) caused by orientational fluctuation of chain segments on the basis of the concept concerning the trans-

formation from the isotropic-to-nematic phase proposed by Doi *et al.* [11].

The detailed observation of light scattered intensity against annealing time was classified into three regions [8,9], based on the annealing experiment when the amorphous PET film was put into a hot oven fixed at a desired temperature and an incident beam of He-Ne gas laser was directed at the film. In the first stage (stage I), the scattered intensity showed insignificant changes. In the second stage (stage II), the logarithm of scattered intensity increased linearly. Such behavior has been analyzed within the framework of the linear theory of SD, determining that the amorphous chains at elevated temperatures were thermodynamically unstable and tended to incur a density fluctuation. In the third stage (stage III), x-ray diffraction and density measurements revealed the initiation of crystallization. The stage I period shortened with increasing annealing temperature; however, any changes could not be confirmed by density, x-ray diffraction, and polarized light scattering measurements.

This paper focuses on conformational changes of amorphous PET chains using a combined experimental and theoretical approach to probe whether the conversion from gauche-to trans-conformation in stage I aids SD at stage II. The amorphous PET film with a thickness of 75 μm was used as a test specimen to obtain a clear Fourier transform infrared (FTIR) absorption peak. The analysis was performed synthetically by using depolarized light scattering, small-

*Author to whom correspondence should be addressed: Tel and Fax: 81-742-20-3462; m-matsuo@cc.nara-wu.ac.jp

angle x-ray scattering (SAXS), wide-angle x-ray diffraction (WAXD), and FTIR. Such systematic analysis represents the first effort of studying crystallization of amorphous PET film during the induction period.

Based on the synthetic analysis, theoretical calculations were carried out to determine whether the conformational change in stage I plays an important role as a driving force in developing molecular ordering to promote the molecular coagulation in stage II and subsequently crystallization in stage III. In order to achieve this, the orientation distribution function of chain segments with respect to a particular direction between two jointed points was formulated by using a lattice model similar to the concept proposed by Bahar *et al.* [12,13]. The lattice model is related to two features. The first one is the entropic and associated with segmental orientation due to the effect of chain stiffness of Kuhn segments characterized by a rod with a relatively large length-to-width ratio x . The second term is an energetic and associated with thermotropic systems with anisotropic polarizabilities. These two factors contribute to a first-order transition from a relatively disordered to a highly oriented structure without any imposition of an external perturbation. The network chains are assumed to be monodisperse, i.e., composed of the same number m of rigid molecules like rods having an ideal axial ratio x , and the increment of x indicates an increase in transfection of an amorphous chain. By using the orientation function, further theoretical calculations were carried out for light scattering patterns under polarization conditions using a statistical approach. In the proposed model system, two distance correlation functions between two optical elements corresponding to the highly oriented structure were introduced for polar and rotational angles of the optical axes. The theoretical patterns were found to be in good agreement with the patterns observed in stage III. Of course, the theoretical calculation was performed within the framework of Rayleigh-Gans theory, apart from the complicated concept of Mie theory [14,15].

II. EXPERIMENTAL SECTION

Sample preparation. PET bottle grade, ELPET from Elana Co., Torun, Poland, was used in this study. Its molecular weight was $M_w=25\,000$, intrinsic viscosity 0.78 ± 0.02 g/DL, density 1.4 g/cm³, melting point 258 °C, and carbonyl group content below 25 eq/kg. The pellets were dried at 170 °C for 4 h in closed air circulation over molecular sieves to the relative humidity corresponding to the dew point of -40 °C. The PET pellets were melted between two steel plates to prepare thin films. The films were quenched in water to room temperature in order to assure amorphous structure of the films. The quenching was followed by embedded thin layer thermocouple. The recorded cooling curves indicated that the glass-transition temperature of PET was reached within 1.2 s. The film thickness was ~ 75 μm .

FTIR measurement. The time-resolved FTIR measurement in the region of $400\text{--}4000$ cm⁻¹ was performed by an average of 20 scans and a resolution of 2 cm⁻¹. The film was placed into the cell and a desired temperature maintained.

The FTIR spectra were recorded quickly as a function of time and each spectrum was obtained at an interval of 1 min. The measurements were continued for 15 min. After 15 min, the spectra were measured at 5 min intervals because only a slight change in the spectra with time was observed following the initial 15-min period.

Light scattering measurement. The *in situ* time-revolved scattered intensity was measured by using a 632.8 nm He-Ne laser, in which a He-Ne gas laser beam through a polarizer was directed to the specimen and the scattered intensity was detected without an analyzer. To measure the time dependence of scattered intensity, nine photodiodes were set at the desired scattering angle (θ) in order simultaneously to detect the scattering beam at various angles. The specimens were subjected to a rapid temperature jump to the desired temperatures when the fixed specimen was set in a temperature-controlled cell. The time required to achieve the equilibrium temperature was less than 20 s. Hence the change in angular distribution of scattered intensity as a function of time was measured after 20 s. On the other hand, the corresponding scattering patterns were observed on a photoplate under cross-polarization condition using a polarizer and an analyzer. The two experiments were carried out separately by using the same optical bench. Namely, the two specimens cut from the amorphous film were used to carry out the two experiments [$\ell n(I)$ and the patterns], and then a lot of efforts were made to assure the same condition to control the same temperature and the same time scale.

Small-angle x-ray scattering (SAXS) measurement. SAXS intensity distribution was performed by the synchrotron radiation dynamic small-angle x-ray scattering apparatus at BL-15A. The scattering data were collected by a position-sensitive proportional counter (PSPC) in an equatorial direction. The wavelength (λ) of incident x ray was 0.1542 nm.

Wide-angle x-ray diffraction (WAXD) measurement. The x-ray measurements were carried out with a 12 kW rotating-anode x-ray generator (Rigaku RDA-rA) operating at 200 mA and 40 kV. The intensity was detected with a curved position-sensitive proportional counter (PSPC) in an equatorial direction. The x-ray source was monochromatized to Cu $K\alpha$ radiation with a platelike graphite monochromator. The scattering intensity with time was measured in the range of $5^\circ\text{--}35^\circ$ (twice the Bragg angle, $2\theta_B$).

Density measurement. The density was measured at 25 °C by a pycnometer in a mixture of carbon tetrachloride and *n*-heptane as a medium. The weight crystallinity was calculated by using $X_c = \rho_c(\rho - \rho_a) / \rho(\rho_c - \rho_a) \times 100\%$, in which ρ_c and ρ_a are 1.455 and 1.335 g/cm³ as the density of crystal and amorphous phases, respectively.

DSC measurement. The thermal behavior was studied with a differential scanning calorimeter (DSC) (EXSTAR 6000) from Seiko Instrument, Inc. Each film was cut into identical circular shape and the samples, weighing about 10 mg, were placed in a standard aluminum sample pan. The sample was heated at a scanning rate of 1 or 10 °C/min.

Storage modulus. The storage modulus was measured at 95 °C in the frequency range of 0.01–100 Hz by using a viscoelastic spectrometer (VES-F) obtained from Iwamoto Machine Co. Ltd. The length of the specimen between the jaws was 40 mm and the width was ~ 1.5 mm.

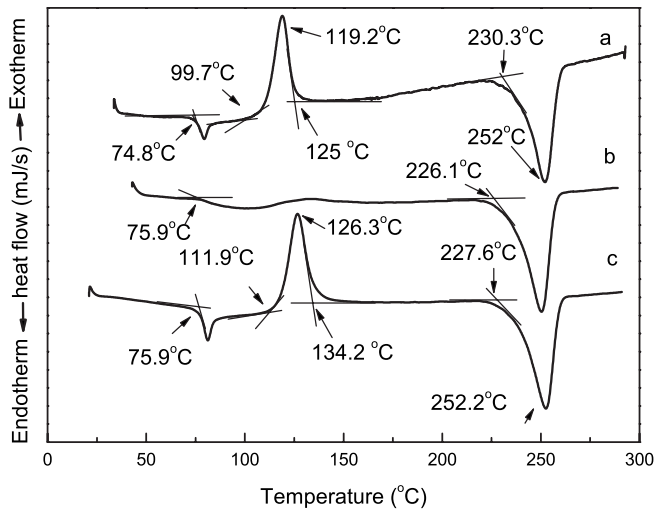


FIG. 1. DSC curve profiles of PET films: (a) The amorphous PET film was heated at a rate of $1\text{ }^{\circ}\text{C}/\text{min}$, (b) the film annealed at $110\text{ }^{\circ}\text{C}$ for 9 min was heated at a rate of $1\text{ }^{\circ}\text{C}/\text{min}$, and (c) the amorphous PET film was heated at a heating rate of $10\text{ }^{\circ}\text{C}/\text{min}$.

III. RESULTS AND DISCUSSION

A. Experimental analysis

DSC scanning thermographs of the amorphous PET film are shown in Fig. 1. Curve (a) reveals three peaks corresponding to a glass-transition temperature peak ($74.8\text{ }^{\circ}\text{C}$), an exothermic peak ($119.2\text{ }^{\circ}\text{C}$), and an endothermic peak ($252\text{ }^{\circ}\text{C}$). The measurements were done at a heating rate of $1\text{ }^{\circ}\text{C}/\text{min}$. From the three peaks, it was found that the initial stages of glass transition, crystallization, and melting occurred at approximately 75 , 100 , and $230\text{ }^{\circ}\text{C}$, respectively. Curve (a) was used to obtain information about the characteristic changes of the amorphous film. The appearance of the sharp peak at $75.9\text{ }^{\circ}\text{C}$ is different from a shoulder associated with the glass temperature of PET reported in the second heating run [16]. Curve (b) measured for the specimen annealed for 9 min at $110\text{ }^{\circ}\text{C}$ shows a shoulder associated with the glass transition. The absence of exothermic peaks indicates that crystallization had occurred at a temperature below $110\text{ }^{\circ}\text{C}$ during the first heating process. Furthermore, the glass transition and crystallization were dependent on the heating rate. That is, curve (c) measured at the heating rate of $10\text{ }^{\circ}\text{C}/\text{min}$ indicated that the beginning of the glass transition and thermal crystallization were 75.9 and $111.9\text{ }^{\circ}\text{C}$, respectively. Curves (a) and (c) indicate that the crystallization mechanism of the amorphous PET film is sensitive to annealing time. Based on the DSC results, the following detailed analysis was carried out in terms of density fluctuation of amorphous phase leading to “quasi-spinodal decomposition.”

Figure 2(a) shows the change in the density as a function of annealing time for the specimen annealed at $95\text{ }^{\circ}\text{C}$. Figure 2(b) shows the logarithmic plots $\ln(I)$ of the scattered intensity of the He-Ne gas laser measured at the scattered vector of $q(q=4.15\times 10^{-4}\text{ }^{\circ}\text{Å}^{-1})$, given by $4\pi n/\lambda \sin(\theta/2)$, with λ , θ , and n being the wavelength of the He-Ne gas laser in the film, the scattering angle, and the refractive index, respectively. The measurements were performed for the specimens

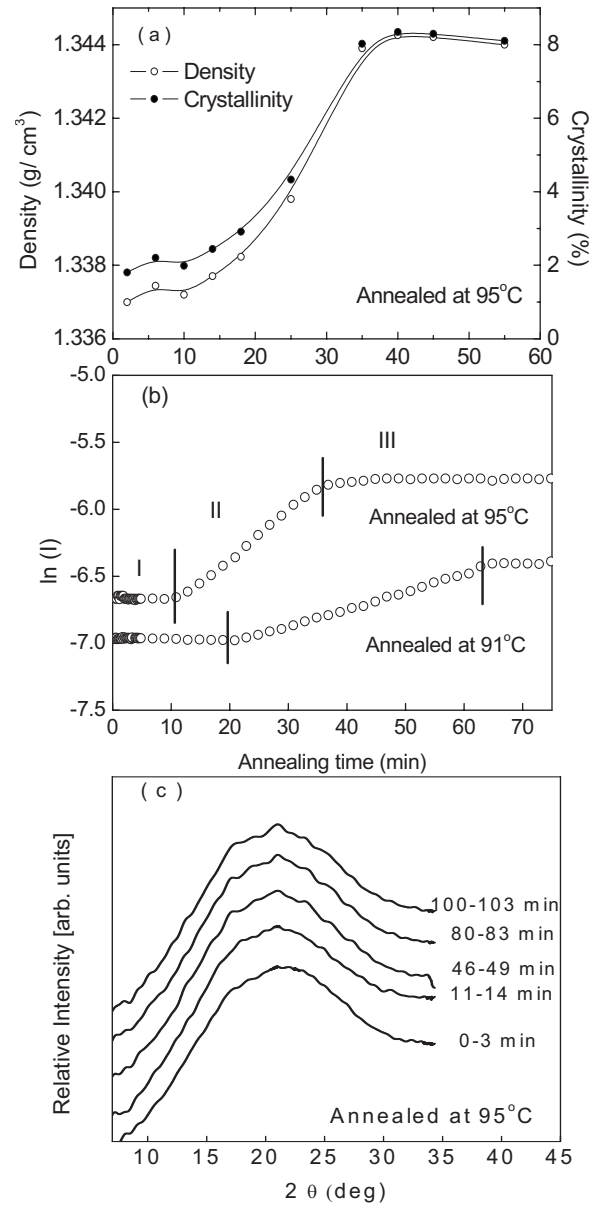


FIG. 2. (a) The density change as a function of annealing time when the amorphous PET film was annealed at $95\text{ }^{\circ}\text{C}$. (b) Change in $\ln(I)$ at $q=4.15\times 10^{-4}\text{ }^{\circ}\text{Å}^{-1}$ measured for the amorphous films annealed at 95 and $91\text{ }^{\circ}\text{C}$. (c) WAXD profiles of the amorphous film annealed at $95\text{ }^{\circ}\text{C}$.

annealed at 91 and $95\text{ }^{\circ}\text{C}$, in which the plots are shifted along the intensity axis to clarify the time dependence of the intensity distribution. Figure 2(c) shows the WAXD curves. The curves of the x-ray intensity, for convenience, are shifted along the intensity axis for a clear view of the evolution of the intensity distribution. The time represented for each x-ray curve indicates the starting time of the accumulation of the x-ray intensity. The intensity distribution curve at $0\text{--}3$ min, for example, denotes the intensity accumulated for 3 min in the range of $0\text{--}3$ min.

As shown in Fig. 2(a), density was observed to increase slightly as the annealing time increased. The densities of the specimens annealed at $95\text{ }^{\circ}\text{C}$ for 10 and 55 min were 1.337 and $1.344\text{ g}/\text{cm}^3$, respectively. The difference in the densi-

ties is clearly very small. In particular, the density maintained a constant value without any change up to 10 min. The detailed analysis reveals that the density of the specimen annealed beyond 10 min increased linearly up to ~ 35 min annealing time and subsequently was essentially static. The increasing behavior of the density is in good agreement with the increasing mode of the corresponding logarithmic plots $\ell n(I)$ in Fig. 2(b), which is classified into three stages: stage I, where $\ell n(I)$ showed insignificant changes; stage II where $\ell n(I)$ increased linearly; and stage III, where the intensity deviates from the linear relationship and asymptotes. At stage I, any increase in $\ell n(I)$ was not observed. Stage I at 91°C was longer than that at 95°C . The increase in $\ell n(I)$ did not appear at 90°C in the given period of annealing time, and the corresponding density for the specimen remained constant within experimental error.

As discussed in previous papers [8,9], the behavior at stage II is similar to the initial stage of phase separation of isotropic amorphous polymer blends by spinodal decomposition (SD). At 95°C , the time at the end of stage II corresponds to the time that the density begins to show no further increase. This means that the increasing behaviors of density and $\ell n(I)$ occur within the same period. As shown in Fig. 2(c), despite the increases in density and $\ell n(I)$, any crystallization by x-ray measurement was not observed at 95°C during the period up to 49 min. The broad peak maintained the same profile independent of the annealing time. Namely, the increases in density and $\ell n(I)$ in stage II may be due to molecular ordering of amorphous chains. However, any change of the amorphous halo due to the molecular ordering was barely detected by WAXD measurements.

To justify the above phenomenon, similar experiments were carried out at 100°C . Figure 3(a) shows the change in density with increasing annealing time for the specimen. The density increased after 5 min had elapsed. This period is shorter than the time (10 min) measured for the specimen annealed at 95°C [see Fig. 2(a)]. The density increased linearly up to 15 min and thereafter deviated from the linear relationship saturating at ~ 30 min. A further increase occurred beyond 40 min. As shown in Fig. 3(b), the observed increase of $\ell n(I)$ was similar to the changes in density. Figure 3(c) shows the measured x-ray diffraction curves. The small diffraction peaks from crystallites were observed by annealing beyond ~ 20 min and the density of the corresponding film was $\sim 1.35\text{ g/cm}^3$ ($\sim 10\%$ crystallinity). The appearance of the broad peak at 100°C also satisfies the initial temperature (99.7°C) of crystallization estimated by DSC [Fig. 1(a)]. The comparison between Figs. 3(b) and 3(c) suggests that the plateau of $\ell n(I)$ beyond 20 min is independent of crystallization, because the appearance of any peak of WAXD intensity distribution was not shorter than 23 min. The peaks became evident with elapsing time, and at 80–84 min the peaks from the (010), ($1\bar{1}0$), and (100) planes were clearly present. Comparison with the results presented in Fig. 2 shows that the periods of stage I and stage II at 100°C were shorter than those at 95°C . In spite of the x-ray diffraction peaks from crystallites by annealing beyond 85 min at 100°C , the corresponding $\ell n(I)$ showed constant intensity in stage III and the increase in $\ell n(I)$ occurred only

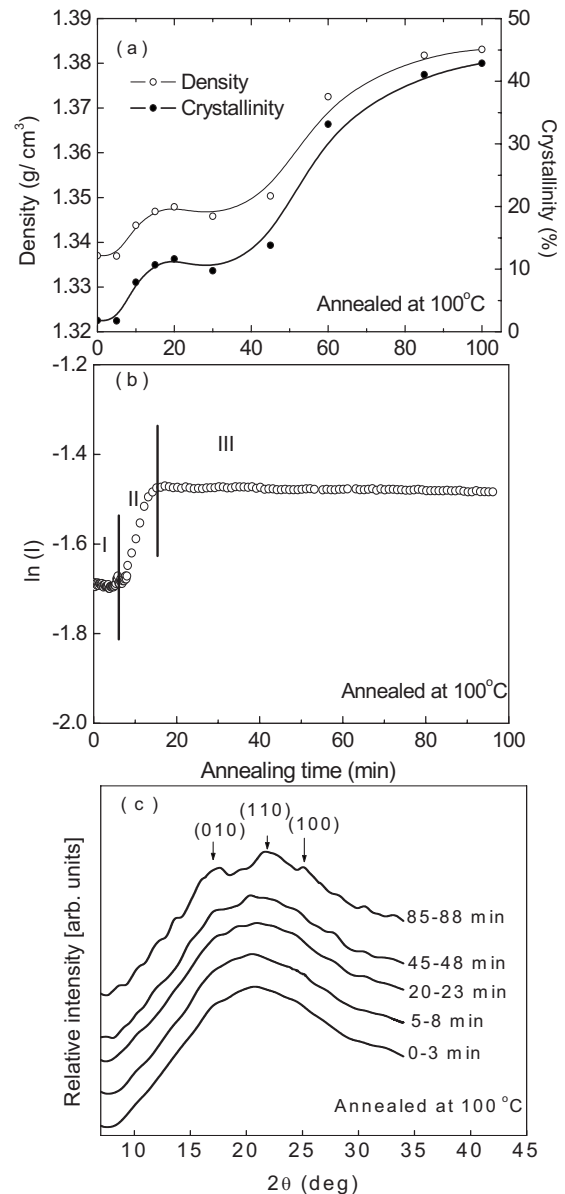


FIG. 3. (a) The density change as a function of annealing time when the amorphous PET film was annealed at 100°C . (b) Change in $\ell n(I)$ at $q=4.15 \times 10^{-4}\text{ \AA}^{-1}$ measured for the amorphous film annealed at 100°C . (c) WAXD profiles of the amorphous film annealed at 100°C .

in stage II. Of course, the albescent phenomenon of the film was not observed visually by annealing beyond 85 min at 100°C . This indicates that the optical density fluctuation between polymer-rich and -poor phases in stage II occurred in a scale larger than the wavelength of visible light, but the crystallites by further chain coagulation in the polymer-rich phase in stage III occurred in a scale smaller than the wavelength.

To further understand the plateau of $\ell n(I)$, SAXS measurements were carried out during the annealing process at 100°C . SAXS measurements at 95°C were not feasible because of the weak SAXS intensity with considerable noise. This is due to the very thin film thickness that was used for the IR measurements. Figure 4 shows the results at 100°C ,

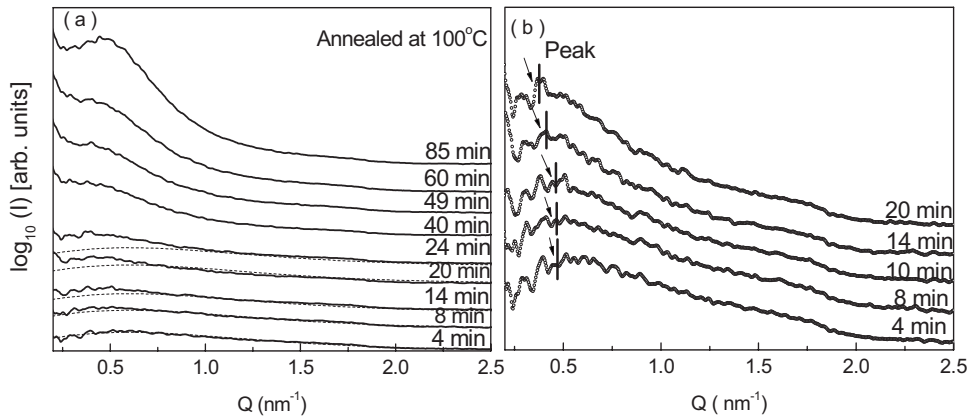


FIG. 4. (a) SAXS intensity profiles of the amorphous PET annealed at 100 °C. (b) The enlarged SAXS profiles in the time range shorter than 20 min.

in which the curves in Fig. 4(b) are an enlargement of the first 20 min for the curves presented in Fig. 4(a). The modification of the SAXS intensity was carried out using the same estimation method as Imai *et al.* [2]. The relative intensity $\ln(I)$ using a logarithmic scale was carried out as a function of Q [$= (4\pi/\lambda)\sin\theta$], where λ is the wavelength of the radiation in the medium, and θ is half of the scattering angle. The scattered intensity is shifted along the intensity axis to clearly view the evolution of the intensity distribution. The SAXS peak magnitude increases with increasing annealing time even in the period before the appearance of the crystalline peak in the WAXD curves. From the peak top, the long period of the specimens annealed for 4–10, 14, and 20 min was calculated to be 13.4, 15.3, and 16.5 nm, respectively. This indicates that long-range order develops prior to crystallization [17]. This phenomenon shall be discussed in addition to the statistical analysis of polarized light scattering discussed later (see Figs. 13 and 14). The peak magnitude increased as time proceeded and the maximum position shifted to a lower degree. Since the SAXS intensity was very weak, the precise analysis of the profiles was very difficult for the stage I period [see Fig. 3(b)]. At periods shorter than 10 min, the scattering peak did not move with elapsing time. This indicates that the scale wavelength of density fluctuations keeps a constant value and the magnitude of the fluctuation increases. On the other hand, at time scale >14 min, the scattering maximum shifted toward a smaller angle Q with an increase in the maximum intensity. Accordingly, the time scale <10 min may correspond to the initial stage (stage II) of the spinodal decomposition, since the peak in-

tensity increased with time at the same position of Q . No WAXD peak actually appeared for the first 20 min [see Fig. 3(c)]. The time scale >14 min corresponds to the later stage (stage III) as pointed out by Imai *et al.* [2] based on Furukawa's scaling theory [18], and the dull diffraction peak appeared beyond 45 min marking the initiation of crystallization. Thus the SAXS profiles indicate that stage III corresponding to the deviation from the linear relationship between $\ln(I)$ versus time in Figs. 2(b) and 3(b) is thought to be associated with the latter stage of spinodal decomposition and the initiation of crystallization with further molecular ordering.

Figure 5 shows typical time evolution of the scattered light intensity at various q values when the sample was isothermally annealed at temperatures that prohibit crystallization but provide an increase in density. The temperature dependence of the refractive index could be neglected within experimental error in the given temperature range examined. Stage I became shorter and the slope at stage II became sharper as the temperature was increased. As discussed previously, the relationship of $\ln(I)$ versus time can be analyzed by the linear theory of the initial stage of spinodal decomposition [19,20]. However, the present system is only one component, different from the phase separation of two components such as a blend of film and gels (polymer and solvent). Interestingly, this behavior detected by a He-Ne gas laser with a wavelength longer than 600 nm is attributed to optical density fluctuation of amorphous chains in the large scale. However, in stage II, the level of density fluctuation detected by SAXS measurements at 100 °C is not sensitive in com-

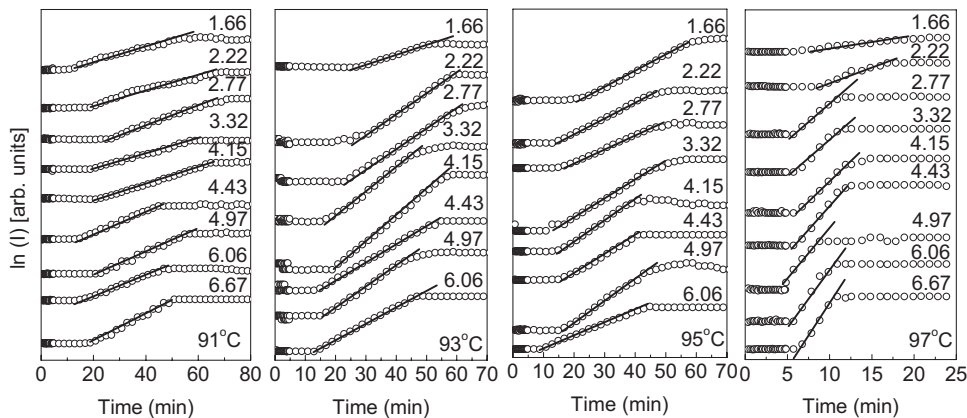


FIG. 5. Logarithm plots of the scattered intensity against time at various q values after the initiation of spinodal decomposition observed for the amorphous PET films. The films were annealed at the indicated temperature.

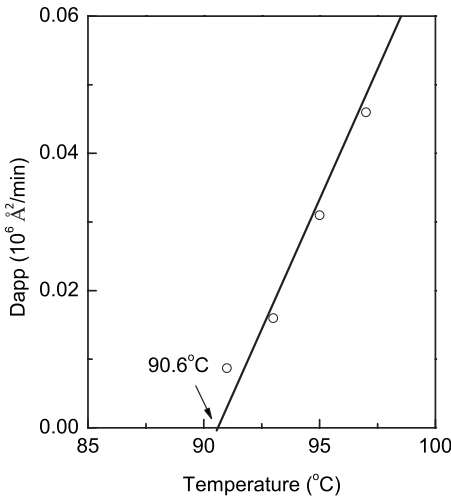


FIG. 6. Temperature dependence of $D_{app}=R(q)/q^2|_{q=0}$ from which the spinodal temperature T_s was deduced. The data were analyzed in stage II.

parison to the level of optical density fluctuation detected by SALS. This means that the gradient of density fluctuation occurred at a very large scale such as the wavelength level of He-Ne gas laser. This is due to the fact that the density fluctuation by chain diffusion provided very large chain rich phases and the additional dense chain packing region detected by SAXS appeared locally in the large rich phases. The essential reason, however, remains unresolved.

Based on the concept of the initial stage of the spinodal decomposition as mentioned by Cahn [19,20], the temperature dependence of the apparent diffusion coefficient, D_{app} , can be obtained in accordance with the procedure described elsewhere [8]. The result is shown in Fig. 6. The spinodal temperature (T_s) is 90.6 °C. Here, $\ln(I)$ and the density were constant beyond 24 h, when the specimens annealed at a constant temperature less than T_s . Certainly, we confirmed that the linear increase of $\ln(I)$ at temperatures lower than T_s did not appear in the given time scale in Figs. 1–5, indicating our reasonable estimation.

Now, it is of interest to consider the driving force arising from the linear increase in $\ln(I)$ against time in stage II. The linear increase certainly occurred suddenly after stage I. Accordingly, the conversion from gauche- to trans-conformation at stage I was performed under the annealing process by *in situ* FTIR measurements in order to clarify what happened in stage I.

Figure 7 shows FTIR spectra in the range of 800–1075 and 1320–1500 cm^{-1} , measured for the films annealed at 95 and 105 °C. The measurements were done at the indicated annealing time. The assignment of the infrared peaks of PET has been discussed in various publications [3,10,21–26]. Although there were some discrepancies with peak positions, the peaks in the present paper were assigned according to Boerio *et al.* [25,26]. Many absorption peaks contribute to gauche-trans pairings that arise from the vibration of the glycol moiety. The absorption peaks at 1453 and 1471 cm^{-1} are related to gauche and trans contributions of CH_2 bending,

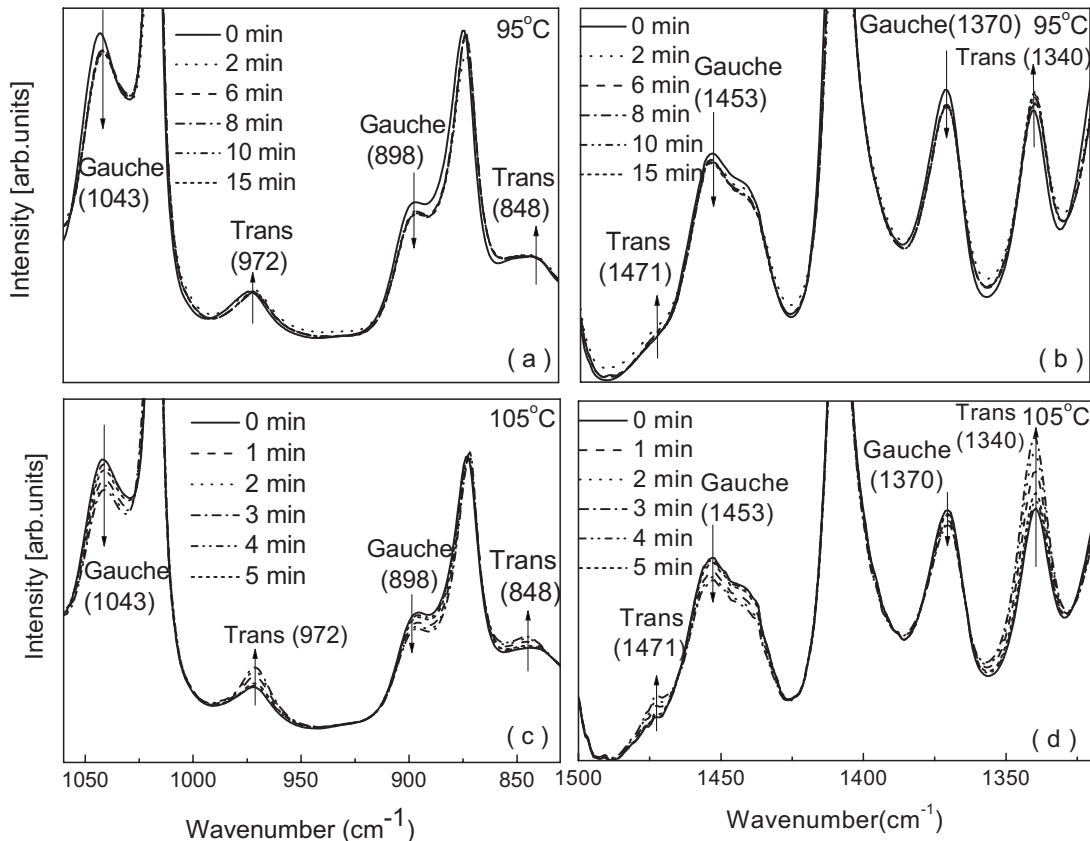


FIG. 7. The real FTIR peak curves at the indicated annealing time for the amorphous PET films annealed at 95 and 105 °C.

respectively; the peaks at 1370 and 1340 cm^{-1} represent gauche and trans of CH_2 wagging; the peaks at 1043 and 972 cm^{-1} represent gauche and trans C-O stretching; and the peaks at 898 and 848 cm^{-1} represent gauche and trans CH_2 rocking.

It is seen that as the annealing time was prolonged, the intensity of the 1340 cm^{-1} band increased, whereas the absorbance reduction of the 1370 cm^{-1} band became relatively smaller as the annealing time was prolonged. The intensity of the 1340 cm^{-1} band increased, whereas the absorbance of the 1370 cm^{-1} band decreased. This can be attributed to the difference in the absorption coefficients of these two bands [21,23]. From this figure, we can find that with increasing annealing time, the trans-fraction increased while the gauche-fraction decreased. This tendency was more significant at 105 °C. Among the several pairs, the absorption bands at 1340 and 1370 cm^{-1} are an effective quantitative approach to measure the conversion from gauche-to trans-conformation.

Accordingly, the transition phenomenon is estimated by using the following equation [27–29]:

$$T = A_{1340}/(A_{1340} + 6.6A_{1370}), \quad (1)$$

where A_{1340} and A_{1370} are the areas of the absorption bands associated with the trans- and gauche-fractions, respectively.

Figure 8 shows the results, where (a) shows the curves at the temperatures up to 105 °C and (b) shows the curves at the temperatures in the range 100–120 °C. In the annealing process, the trans-fraction increased and reached a steady state after a certain period, but the equilibrium values are different and dependent on the annealing temperature. The trans-fraction at the equilibrium state was higher as the annealing temperature was increased. This phenomenon is due to the mobility of molecular chains becoming more active as the annealing temperature increases up to the initiation of crystallization. The results showed that for the same annealing time, a higher temperature can accelerate the gauche to trans conversion. This supports the results for isothermal crystallization (in the temperature range of 100–125 °C) by DSC measurements.

The FTIR spectra in Fig. 7 and DSC curves in Fig. 1 indicated that annealing at 75 and 80 °C beyond the glass-transition point (74.8 °C) caused a slight increase in the trans conformation content of PET chains with the annealing time yet does not cause any noticeable increase in crystallization. In contrast, annealing at 85–100 °C caused an increase in the trans-fraction as shown in the FTIR spectra and is static beyond 5 min. The period (shorter than 5 min) corresponds to stage I as shown in Fig. 5. Of course, the trans-gauche conversion is independent of an increase in density at 95 and 100 °C (see Figs. 2 and 3). Such interesting phenomena indicate that an increase in the trans-fraction of amorphous PET chains hardly leads to an increase in crystallinity in stage I. Yet, a further increase in the trans-fraction beyond the critical content promotes the appearance of high-density regions due to the diffusion of amorphous chains [5,28] and facilitates crystallization in these regions.

At high temperatures such as 120 °C, the mobility of the segments was significant to permit rearrangement by seg-

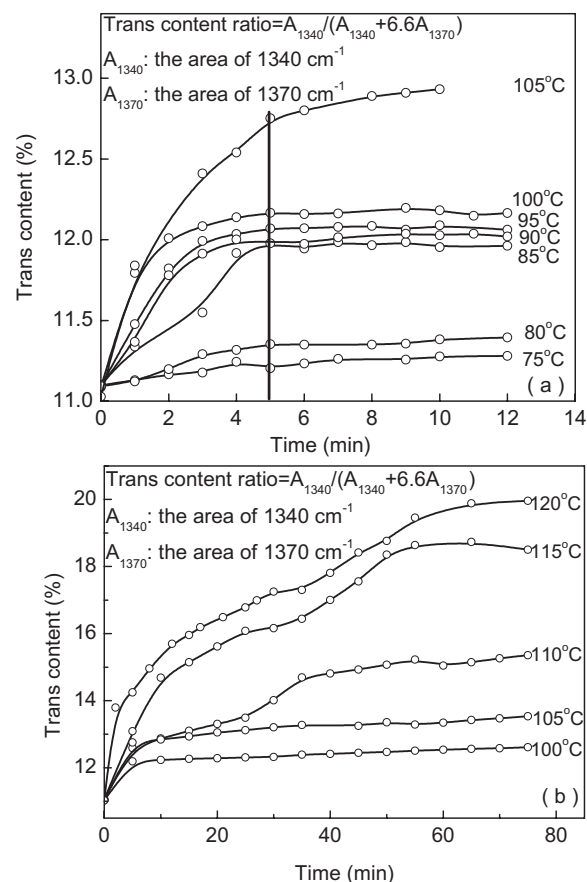


FIG. 8. Trans content of PET chains estimated based on the peak areas measured for 1340 and 1370 cm^{-1} bands, as a function of annealing time at annealing temperature: (a) 75–105 °C; (b) 105–120 °C.

ment motion so that the accelerated conversion from gauche-to-trans conformation promotes noticeable crystallization as shown in Fig. 8(b). This observation satisfies the DSC result, which showed the exothermic peak at ~ 119 °C.

Here it is of interest to consider the mechanical property with increasing annealing time in stage I. Certainly, in stage I, the density was constant in spite of an increase in the trans-fraction. To check whether an increase in the trans-fraction influences the chain rigidity, the storage modulus was measured as a function of frequency because the bulk Young's modulus is related to elastic stiffness of a chain. Figure 9 shows the storage modulus measured at 95 °C as a function of frequency. The indicated annealing time is the starting time of the measurement. About 3 min was required to fix the film in the equipment. Subsequently, 5 min, for example, corresponds to ~ 8 min and the indicated time is in the range of stage I as shown in Fig. 2. The storage modulus increased slightly as the annealing time increased. This means that the increase in the trans-fraction promotes chain rigidity. Accordingly, we shall use a modified lattice model [30,31] proposed by Bahar *et al.* [13] to analyze the orientation of chain segments as a function of length-to-width ratio x assuming a rod corresponding to the rigid chain segments, since the model characterizes chain rigidity with increasing x . This shall be discussed later in Fig. 12.

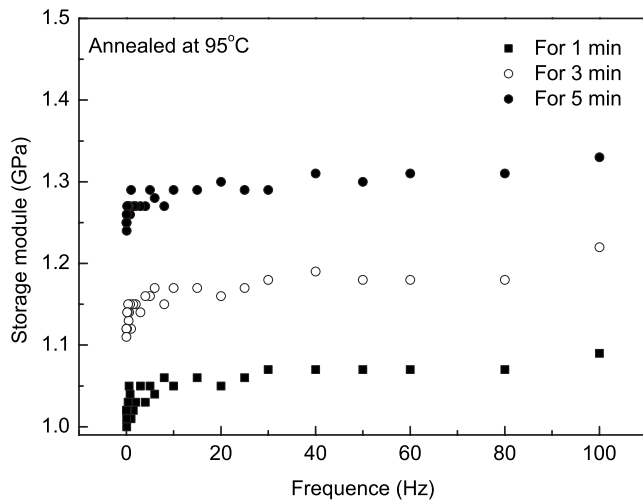


FIG. 9. The storage modulus against frequency measured for PET films annealed for 1, 3, and 5 min at 95 °C.

Returning to Fig. 8(a), the increment of trans-fraction with elapsing time was clearly seen at 85 °C, which was lower than the quasi-spinodal temperature (91 °C). This difference is due to the experimental error on estimating spinodal decomposition, which must be taken into consideration because of the slight difficulty in estimating the slope obtained from plots of $\ln(I)$ versus time. Nonetheless, it is obvious that the driving force of the density fluctuation of the amorphous PET film is closely related to the gauche-trans conversion.

Figure 10 shows the change in $\ln(I)$ at $q=4.15 \times 10^{-4} \text{ \AA}^{-1}$ and the appearance of the SALS patterns under H_v polarization conditions with elapsing annealing time. The measurements were done at 95, 100, and 105 °C shown in Figs. 10(a)–10(c), respectively. The H_v pattern did not appear in stage I and stage II. The very indistinct pattern appeared at the beginning of stage III. This indicated aggregation of amorphous chains and amorphous chain ordering with respect to a particular direction, but the scattering patterns are very poorly defined with very weak scattered intensity. This means that the average size of the formed aggregations by chain ordering is smaller than the wavelength of He-Ne gas laser. However, the scattering profile becomes larger and the intensity becomes stronger at stage III beyond 3 h at 95 °C, 2 h at 100 °C, and 1 h at 105 °C. This observation indicates that the average size of the aggregation is in the light wavelength level. This was especially the case for the indistinct pattern from the film annealed at 105 °C, which became clearer and showed an X-type indicating the azimuthal angular dependence (μ -dependence). This indicates that molecular ordering was pronounced and the correlation between scattering elements was stronger. This tendency can be explained clearly by FTIR results denoting gauche-trans conversion of amorphous PET chains. Incidentally, any clear superstructure could not be observed in stage III under polarized microscopy in the preliminary experiment. Accordingly, it is conclusive that the trans-gauche conversion of amorphous PET chains in stage I plays an important role as a driving force for the density fluctuation by chain diffusion in accordance with quasi-spinodal decompo-

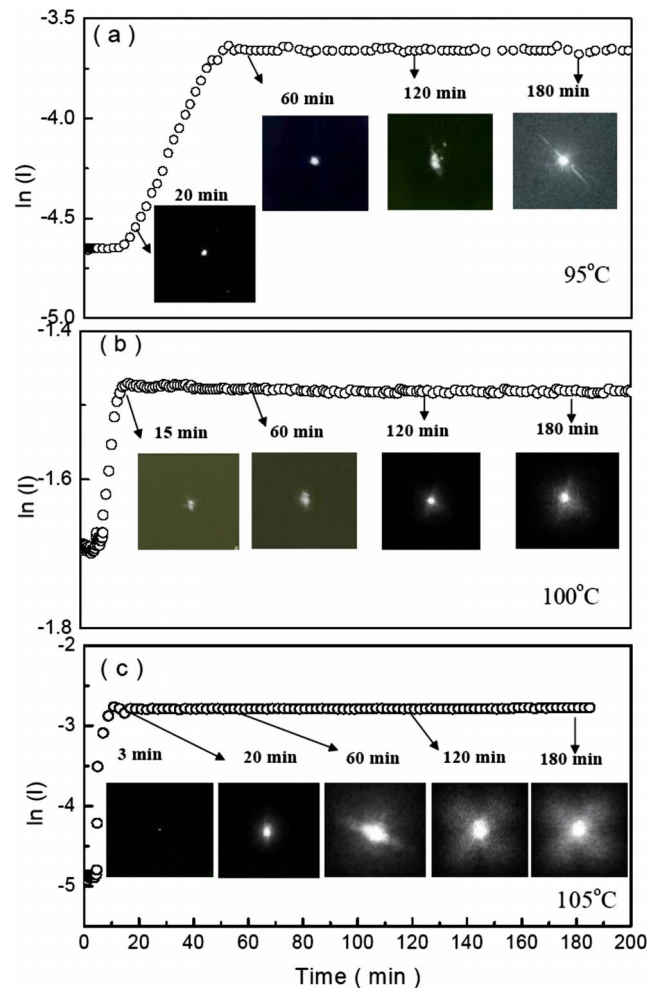


FIG. 10. (Color online) Change of $\ln(I)$ against annealing time at $q=4.15 \times 10^{-4} \text{ \AA}^{-1}$ and the H_v SALS patterns observed at the indicated annealing times.

sition. If this is the case, the molecular orientation is thought to occur locally, although the average orientation of total PET chains is undoubtedly random in a film. Here, a PET chain will orient with respect to a particular direction and then some of the chains coagulate, and this allows the formation of a polymer denser phase to initiate crystallization.

Interestingly, the increase in $\ln(I)$ did not occur in stage III in spite of the clearer observation of the H_v patterns with elapsing time. Such a phenomenon has been observed usually for PET films with thickness of $\sim 200 \mu\text{m}$ [8] and for ultrahigh molecular weight polyethylene under gelation process [32]. This reason remains an unresolved problem.

B. Theoretical analysis for orientation of rigid molecules by the lattice model

To simplify the present concept, the orientation distribution of chain segments with respect to a particular direction is formulated theoretically by using a model [30,31] similar to the concept proposed by Bahar *et al.* [13]. They proposed a lattice model relating to two factors: (i) segmental orientation associated with the effect of chain stiffness of Kuhn

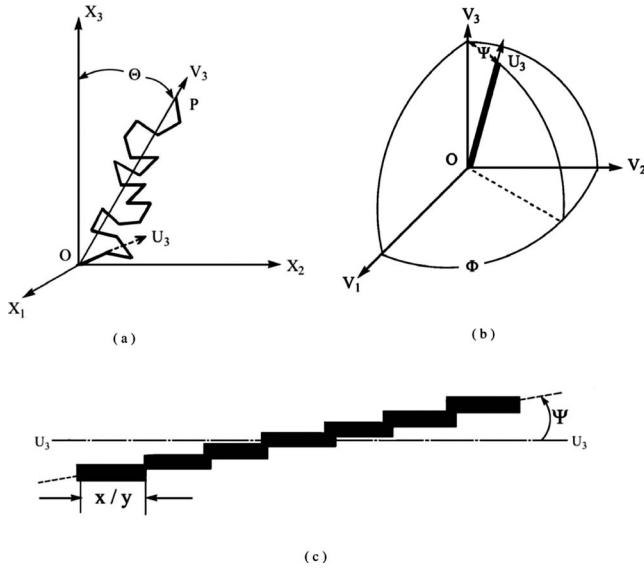


FIG. 11. (a) Network chains of Kuhn segments between the two successive cross-linked points O and P . (b) Polar angle ψ and azimuthal angle Φ specify the orientation of a rigid segment of a chain (U_3) with respect to the Cartesian coordinate $0-V_1V_2V_3$. (c) Division of the rigid segment into submolecules.

segments characterized by a rod with a relatively large length-to-width ratio x , and (ii) thermotropic systems with anisotropic polarizabilities. These entropic and energetic characters contribute to the high orientation of amorphous chain segments without any imposition of an external perturbation. The network chains are assumed to be monodisperse, i.e., composed of the same number m of rigid molecules like rods having an ideal axial ratio x . In the present concept, the increment of x may quantitatively reflect an increase in the trans-fraction of an amorphous chain.

Figure 11(a) shows an illustrative network chain consisting of Kuhn segments (i.e., freely jointed rods) between two successive cross-linked points O and P . The V_3 axis parallel to the direction between the two cross-link points is specified with respect to the Cartesian coordinate $0-X_1X_2X_3$ with the space of the film. The X_1 axis is the film thickness direction and the X_2 and X_3 axes are parallel to the film surface, in which Θ is the polar angle of the V_3 axis with respect to the X_3 axis. In the present system, the V_3 axis is random with respect to the X_3 axis (also in the bulk specimen). In Fig. 11(b), the U_3 axis denoting the direction of a rod containing submolecules is defined by the polar angle Ψ and the azimuthal angle Φ with respect to the Cartesian coordinate $0-V_1V_2V_3$. Following Flory *et al.* [33], the accommodation of the rod in the lattice within the k -th solid angle is achieved through its representation by a sequence of $y_k = x \sin \Psi_k$ submolecules, each occupying x/y_k sites and oriented along the U_3 axis, as shown in Fig. 11(c). Thus y_k characterizes the given rod. This term is expressed in terms of Ψ_k and Φ_k as

$$y_k = x \sin \Psi_k (|\cos \Phi_k| + |\sin \Phi_k|) \quad (2)$$

for the rod (the U_3 axis) exhibiting a preferential orientation with respect to the V_3 axis. Accordingly, the values of y_k increase as the rod becomes disordered, as pointed out by

Erman *et al.* [12]. In their model system, the preferred direction corresponds to an arbitrary one between the two successive cross-linked points. The rods orient to the direction without any external excitation in order to minimize the free energy of the given system when the length x of the Kuhn segment is beyond the critical value. Considering the Helmholtz free energy, this is undoubtedly reasonable for highly oriented chains to form a liquid-crystal system and for highly oriented hard rods dispersed in a dilute solution. The preferred axis was chosen along the direction between the two cross-linked points as discussed in previous papers [30,31]. The treatment is similar to that of freely jointed chains of finite length represented by the distribution of Langevin.

Following Bahar *et al.* [13], which was proposed in the concept by Flory [34], the amorphous PET with monodisperse chains is buried in the sites and the excess sites remain voids. This is based on the assumption that the volume of void is equal to solvent molecules. If this is the case, the present model is similar to the lattice model representing the arrangement of polymer chains and solvent molecules in a liquid-crystal system [34].

The total configuration partition function of a system of n_2 polymer and n_1 voids (instead of solvent molecules) in a lattice model consisting of n_o sites ($n_o = n_1 + mxn_2$) can be given by $Z_m = Z_{\text{comb}} Z_{\text{orient}}$, where Z_{comb} and Z_{orient} are the combinational part and orientational part of the partial function. The configuration partition function Z_m is used in the evaluation of the Helmholtz free energy change of mixing according to

$$\Delta A_m = -k_B T \ell_n Z_m, \quad (3)$$

where k_B is the Boltzmann constant and T is the absolute temperature. According to the derivation similar to Erman *et al.* [12], $-\ell_n Z_{\text{comb}}$ is given by

$$-\ell_n Z_{\text{comb}} = n_1 \ell_n v_1 + n_2 \ell_n \left(\frac{v_2}{mx} \right) - (n_1 + n_2 m \bar{y}) \ell_n \left[1 - v_2 \left(1 - \frac{\bar{y}}{x} \right) \right] + n_2 (m \bar{y} - 1) - n_2 (m - 1) \ell_n (z - 1). \quad (4)$$

On the other hand, the orientational partition function Z_{orient} is given by

$$Z_{\text{orient}} = \prod_{j=1}^{n_2} m! \prod_k \frac{\omega_k^{n_{j,k}}}{n_{j,k}!} = \prod_{j=1}^{n_2} n_{j,k} \prod_{j=1}^{n_2} \frac{\omega_k^{n_{j,k}}}{n_{j,k}!}, \quad (5)$$

where ω_k is the fractional range of the solid angle replaced by $(1/4\pi) \sin \Psi_k d\Psi_k$. Here, the equilibrium distribution of segments among different orientations is obtained by minimizing the free energy of the system with respect to $n_{j,k}$ (the number of segments of the j -th chain) to find the distribution of the probabilities of different configurations of segments in the network between the two cross-link points. The imposition of external constraints requires the use of Lagrange multipliers to minimize the free energy. Thus,

$$\frac{\partial}{\partial n_{j,k}} [\ell_n Z_m] = 0, \quad (6)$$

$$\sum n_{j,k} = m, \tag{7}$$

$$\sum n_{j,k} \cos \Psi_k b = h, \tag{8}$$

where b is the length of a segment and h is the distance between two cross-link points. From Eqs. (7) and (8), we have

$$\alpha \sum \delta n_{j,k} = 0, \tag{9}$$

$$\beta \sum \cos \Psi_k \delta n_{j,k} = 0. \tag{10}$$

Substituting Eqs. (9) and (10) into Eq. (6), the equation takes the form

$$\frac{n_{j,k}}{m\omega_k} = \exp[\beta \cos \Psi_k - \alpha y_k - 1]. \tag{11}$$

Considering the difficulty in carrying out a double integration to determine β , the problem can be simplified to a considerable extent by preaveraging Φ_k dependence prior to numerical integration over Ψ_k . Accordingly, y_k is given as $(4x/\pi)\sin \Psi_k$ and the orientation distribution function of Eq. (11) can be represented by omitting the dummy subscript k as follows:

$$f(\Psi) = Q_o \exp\left(\beta \cos \Psi - \frac{4ax}{\pi} \sin \Psi - 1\right), \tag{12}$$

where

$$a = -\ell n \left[1 - v_2 \left(1 - \frac{\bar{y}}{x} \right) \right]. \tag{13}$$

Q_o is a normalized constant.

According to Bahar *et al.* [13], the lattice model for segmental orientation can be applied to the thermotropic system with anisotropic polarizabilities. The treatment was first proposed by Flory for thermotropic systems with orientation-dependent interactions, and the theory is useful to explain the transition between crystallites, nematic, and isotropic phases. The theory contains a factor of energetic character that contributes to a first-order transition from a relatively disordered to a highly oriented structure. In the present paper, the energetic character was adopted to promote the orientation of amorphous chain segments with respect to the direction connected between cross-linked points.

In this case, the new orientation distribution can be written as

$$f_T(\Psi) = Q_o \exp\left[\beta \cos \Psi - \frac{4xa}{\pi} \sin \Psi + SH^{-1}P_2(\cos \Psi)\right], \tag{14}$$

where

$$S = \frac{\int_0^\pi f_T(\Psi) P_2(\cos \Psi) \sin \Psi d\Psi}{\int_0^\pi f_T P_2(\cos \Psi) \sin \Psi d\Psi}. \tag{15}$$

In Eq. (14),

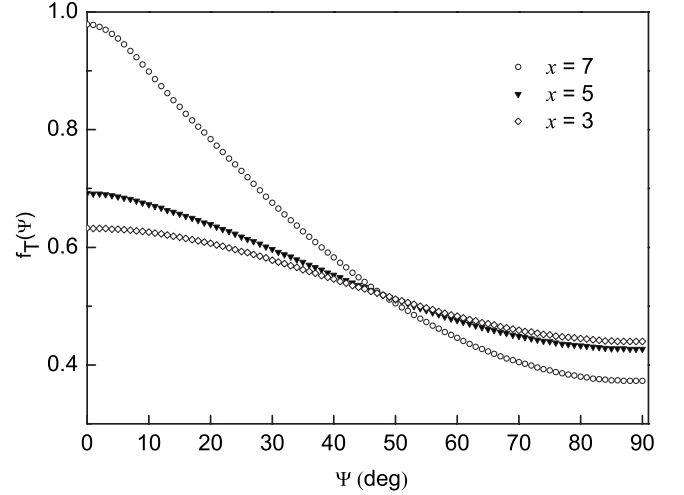


FIG. 12. Orientation distribution function calculated by Eq. (14) at $x=7, 5$, and 3 .

$$H = \frac{kT}{x} \left[\frac{Cz_C(\Delta\alpha)^2}{r^{*6}} \right]^{-1}, \tag{16}$$

where z_C is the number of first neighbors surrounding the segment, $\Delta\alpha$ is the mean anisotropy of all segments, r^* is the distance between subsegments for dense packing, and C is a constant.

Figure 12 shows the orientation distribution function calculated by Eq. (14). The function becomes sharper with increasing x , which reveals the rigidity of chain segments. This indicates that the rigid chains orient predominantly in a particular direction. The numerical calculation was done at $H^{-1}=2$, and $m=20$. The theoretical curves support such experimental results that the gauche-trans conversion becomes more pronounced as the annealing temperature is increased. This means that the conversion from gauche-to-trans conformation promotes a driving force to cause the aggregation of ordered chains by density fluctuation associated with quasi-spinodal decomposition. This corresponds to the preferential orientation of rods corresponding to the rigid chain segments with respect to the direction connected with two cross-linked points. Of course the total rod (and chain) orientation within the specimen must be random in the film.

C. Statistical approach for light scattering patterns under polarization condition

According to our previous paper [35], the H_v pattern that appeared in the gel was analyzed in terms of the correlation distance between anisotropic optical elements by using a statistical approach slightly different from the previous mathematical treatment. The optical axes of the scattering elements with the correlation distance were assumed to be random in a specimen. However, in the present case, the Kuhn segments with distance correlation are oriented in the preferred direction connected between two cross-linked points. Figure 13(a) shows the schematic diagram, in which the polar angle of the optical axis with respect to the V_3 axis is represented as ω instead of Ψ , since ω has been the usual

symbol for SALS notation. In this model system, an incident beam detected by a unit vector s_o is propagated along the X_1 direction and the scattered vector denoted as a unit vector s' is detected as a function of the scattering angle θ and azimuthal angle μ taken from the vertical direction X_3 . Figure 13(b) shows a crystallization model in a polymer phase at stage III appeared by density fluctuation based on the concept that PET crystallites in an undrawn film usually take folded crystals. This model is proposed to explain the following: (i) the relationship between Fig. 13(a) and Fig. 11(b), and (ii) the appearances of H_v scattering patterns in Fig. 10 and the peak profile of SAXS intensity distribution in Fig. 4. The distance r_{i+1} between neighbor optical elements [i th and $(i+1)$ th] in Fig. 13(b) corresponds to the long period detected by a SAXS peak, the length being 13 nm, while the strong correlation associated with distance r_{ij} between the i th and j th elements (not the neighbor crystallite) provides the X-type lobes of the H_v light scattering patterns. If this is the case, the long-range order prior to crystallization develops in the wavelength of visible light, as discussed before. In the present model, a rod in Fig. 13(b) means that shown in Fig. 11(b) corresponds to a folded length to form crystallites in stage III, in which the number of loops in a folded crystal is assumed to be approximately the number of rods, m . The optical axes of the j th and i th elements of a PET chain segment are along the U_{j1} and U_{i1} axes and correspond to the direction perpendicular to the benzene ring and different from the chain segment direction U_{j3} and U_{i3} . We shall discuss the reason briefly. The principal refractive index of the PET crystal is estimated in the usual way by assuming the atomic arrangements within the crystal reported by de Daubeny *et al.* [36,37], the values of the bond polarizabilities according to Bunn and de Daubeny [36,37], and by neglecting the uncertain effects of the internal field within the crystal and of secondary bonds upon the principal polarizabilities. On the basis of the principal polarizabilities obtained by the above estimation, the indices along the three principal crystallographic axes are calculated by the Lorenz-Lorentz relation, which is given by Sakaguchi *et al.* [38]. They are estimated as $n_{33}^{co}=1.806$ (along the chain direction), $n_{22}^{co}=1.733$ (perpendicular to the chain direction on the benzene ring), and $n_{11}^{co}=1.398$ (perpendicular to the benzene ring), in which the crystal density is taken as 1.455 g/cm^3 . Then the refractive indices of the amorphous phase, assuming rotational ellipsoidal anisotropy around the a^* axis (corresponding to the direction normal to the benzene ring), are again estimated from the polarizabilities by considering an amorphous density different from that of the crystalline phase. We then have $n_{11}^{am}=1.362$ and $n_{22}^{am}=n_{33}^{am}=1.687$, in which the former is the refractive index along the axis normal to the benzene ring, and the latter are the refractive indices perpendicular to the a^* axis [39].

In accordance with the general concept of polarized light scattering from the system in Fig. 13, H_v scattered intensity is given by [35]

$$I = C \sum_i \sum_j (\mathbf{M}_i \cdot \mathbf{O})(\mathbf{M}_j \cdot \mathbf{O}) \cos[k(\mathbf{r}_{ij} \cdot \mathbf{s})], \quad (17)$$

where the product of the induced dipole moment \mathbf{M}_i in the i th scattering element and polarization direction \mathbf{O} is given by

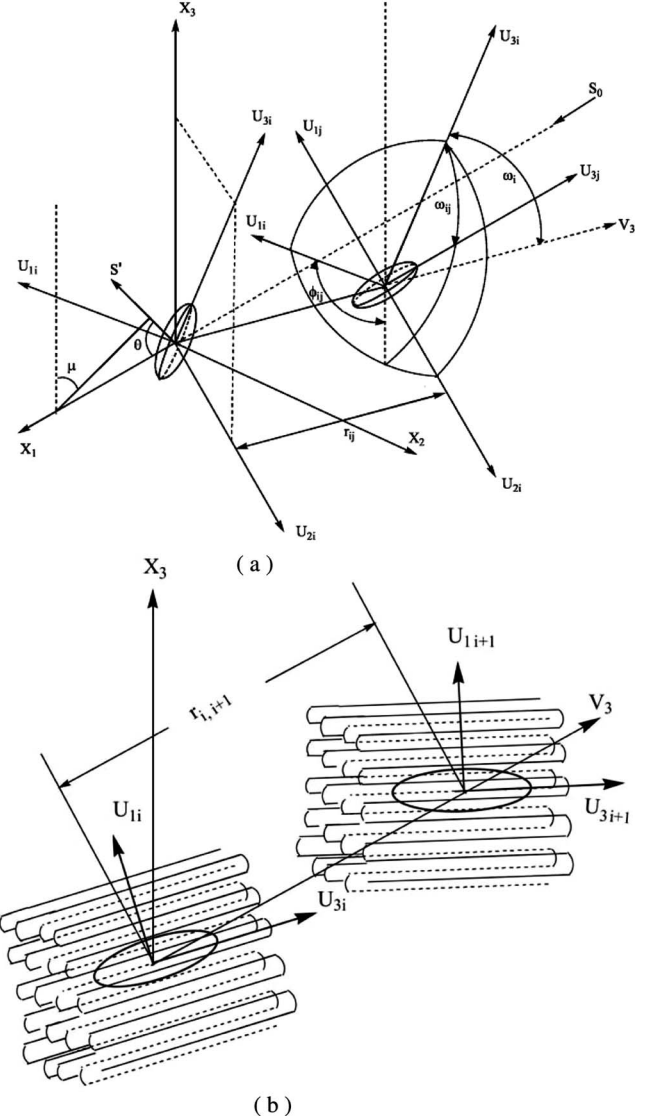


FIG. 13. (a) Optical coordinate system of light scattering concerning the principal polarizabilities of the scattering elements. (b) The crystallization model in a polymer-rich phase at stage III.

$$(\mathbf{M}_i \cdot \mathbf{O}) = \{ \alpha_{i1}(\mathbf{u}_{i1} \cdot \mathbf{k})(\mathbf{u}_{i1} \cdot \mathbf{j}) + \alpha_{i2}(\mathbf{u}_{i2} \cdot \mathbf{k})(\mathbf{u}_{i2} \cdot \mathbf{j}) + \alpha_{i3}(\mathbf{u}_{i3} \cdot \mathbf{k})(\mathbf{u}_{i3} \cdot \mathbf{j}) \} E_o, \quad (18)$$

where \mathbf{u}_{i1} , \mathbf{u}_{i2} , and \mathbf{u}_{i3} are unit vectors along the U_{i1} , U_{i2} , and U_{i3} axes, respectively, representing the three principal axes of the i th scattering element.

As described before, the scattering element of a PET chain is rotationally symmetric with respect to the U_{i1} axis, and may be described by two polarizabilities: $(\alpha_{\parallel})_i$ in the principal direction of the unit vector \mathbf{u}_{i1} and $(\alpha_{\perp})_i$ perpendicular to this direction.

That is, $\alpha_{i2} = \alpha_{i3} = (\alpha_{\perp})_i$ and $\alpha_{i1} = (\alpha_{\parallel})_i$.

The average polarizability of the i th volume element α_i is

$$\alpha_i = \frac{1}{3} [(\alpha_{\parallel})_i + 2(\alpha_{\perp})_i]. \quad (19)$$

When the anisotropy of the i th volume element is specified by $\delta_i = (\alpha_{\parallel} - \alpha_{\perp})_i$, we have

$$(\alpha_{\parallel})_i = \alpha_i + \frac{2}{3} \delta_i, \quad (20)$$

$$(\alpha_{\perp})_i = \alpha_i - \frac{1}{3} \delta_i. \quad (21)$$

The scattered intensity under H_v polarization conditions may be calculated as follows:

$$I_{H_v} = C \sum_i \sum_j \delta_i \delta_j (\mathbf{u}_{1i} \cdot \mathbf{k})(\mathbf{u}_{1i} \cdot \mathbf{j})(\mathbf{u}_{1j} \cdot \mathbf{k}) \times (\mathbf{u}_{1j} \cdot \mathbf{j}) \cos[k(\mathbf{r}_{ij} \cdot \mathbf{s})]. \quad (22)$$

To pursue the theoretical calculation, the U_3 axis is taken as a random rotation around its own axis. After much more complicated mathematical treatment than the previous treatment described in a previous paper [35], H_v scattered intensity is given by

$$I_{H_v} = \int_0^\pi \int_0^\infty \left[g(r)[f(r) - 1]I_1 + f(r)I_2 + \{g(r)[f(r) - 1]I_3 + f(r)I_4\} \cos^4 \frac{\theta}{2} \sin^2 2\mu \right] \cos[hr \cos \alpha] r^2 \sin \alpha dr d\alpha, \quad (23)$$

where I_1 , I_2 , I_3 , and I_4 are given by

$$I_1 = -\frac{1}{32} \left(\cos^4 \alpha - 2 \cos^2 \alpha + 1 - (5 \cos^4 \alpha - 6 \cos^2 \alpha + 1) \cos^2 \frac{\theta}{2} \right) + \frac{1}{384} \left(45 \cos^4 \alpha - 66 \cos^2 \alpha + 13 - 3(75 \cos^4 \alpha - 78 \cos^2 \alpha + 11) \cos^2 \frac{\theta}{2} \right) \langle \cos^2 \omega \rangle - \frac{1}{384} (35 \cos^4 \alpha - 30 \cos^2 \alpha + 3) \left(1 - 5 \cos^2 \frac{\theta}{2} \right) \langle \cos^4 \omega \rangle, \quad (24)$$

$$I_2 = \frac{1}{32} \left(\cos^4 \alpha - 2 \cos^2 \alpha + 1 - (5 \cos^4 \alpha - 6 \cos^2 \alpha + 1) \cos^2 \frac{\theta}{2} \right) - \frac{1}{128} \left(35 \cos^4 \alpha - 30 \cos^2 \alpha + 1 - 5(35 \cos^4 \alpha - 30 \cos^2 \alpha + 3) \cos^2 \frac{\theta}{2} \right) \langle \cos^2 \omega \rangle + \frac{1}{128} (35 \cos^4 \alpha - 30 \cos^2 \alpha + 3) \left(1 - 5 \cos^2 \frac{\theta}{2} \right) \langle \cos^4 \omega \rangle, \quad (25)$$

$$I_3 = -\frac{1}{1536} (35 \cos^4 \alpha - 30 \cos^2 \alpha + 3) (70 \langle \cos^4 \omega \rangle - 45 \langle \cos^2 \omega \rangle + 12), \quad (26)$$

$$I_4 = \frac{1}{256} (35 \cos^4 \alpha - 30 \cos^2 \alpha + 3) (35 \langle \cos^4 \omega \rangle - 30 \langle \cos^2 \omega \rangle + 2). \quad (27)$$

In Eq. (23), the orientation correlation function $f(r)$ associated with the polar angle ω_{ij} between two optical axes is defined by Stein and Wilson [39], and it is given as a Gaussian function in the present paper as follows:

$$f(r) = \left\langle \frac{3 \cos \omega_{ij} - 1}{2} \right\rangle = \exp\left(-\frac{r^2}{a^2}\right). \quad (28)$$

The azimuthal angle ϕ_{ij} , which makes a projection of the j th optical axis onto a plane perpendicular to the optical axis of the i th element, is also given as a correlation distance between the two elements, and it is given as follows:

$$g(r) = \langle 2 \cos^2 \phi_{ij} - 1 \rangle = \exp\left(-\frac{r^2}{b^2}\right). \quad (29)$$

Here ω is the polar angle of the principal axis (corresponding to a chain segment) with respect to the direction connecting between the centers of gravities, and the second and fourth moments are given by using the orientation function of $f_T(\omega)$ as follows:

$$\langle \cos^2 \omega \rangle = \int_0^\pi f_T(\omega) \cos^2 \omega \sin \omega d\omega \quad (30)$$

and

$$\langle \cos^4 \omega \rangle = \int_0^\pi f_T(\omega) \cos^4 \omega \sin \omega d\omega. \quad (31)$$

As described before, $f_T(\cos \omega)$ in Eqs. (30) and (31) corresponds to $f_T(\cos \Psi)$ in Eq. (14).

When ω is random, Eq. (23) reduces to

$$I_{H_v} = \int_0^\pi \int_0^\infty \left\{ f(r) \left(-\frac{1}{960} (5 \cos^4 \alpha + 30 \cos^2 \alpha - 27) + \frac{1}{192} \cos^2 \frac{\theta}{2} (5 \cos^4 \alpha + 6 \cos^2 \alpha - 3) \right) + g(r) [1 - f(r)] \right. \\ \times \left(-\frac{1}{1440} (15 \cos^4 \alpha - 30 \cos^2 \alpha + 31) + \frac{1}{96} \cos^2 \frac{\theta}{2} (5 \cos^4 \alpha - 6 \cos^2 \alpha + 1) \right) - \frac{1}{768} \{ 2g(r) [1 - f(r)] + f(r) \} \cos^4 \frac{\theta}{2} \sin^2 2\mu (35 \cos^4 \alpha - 30 \cos^2 \alpha + 3) \\ \left. \times \cos[hr \cos \alpha] r^2 \sin \alpha dr d\alpha. \right\} \quad (32)$$

If ϕ_{ij} is random, $g(r)$ becomes zero. In this case, we have

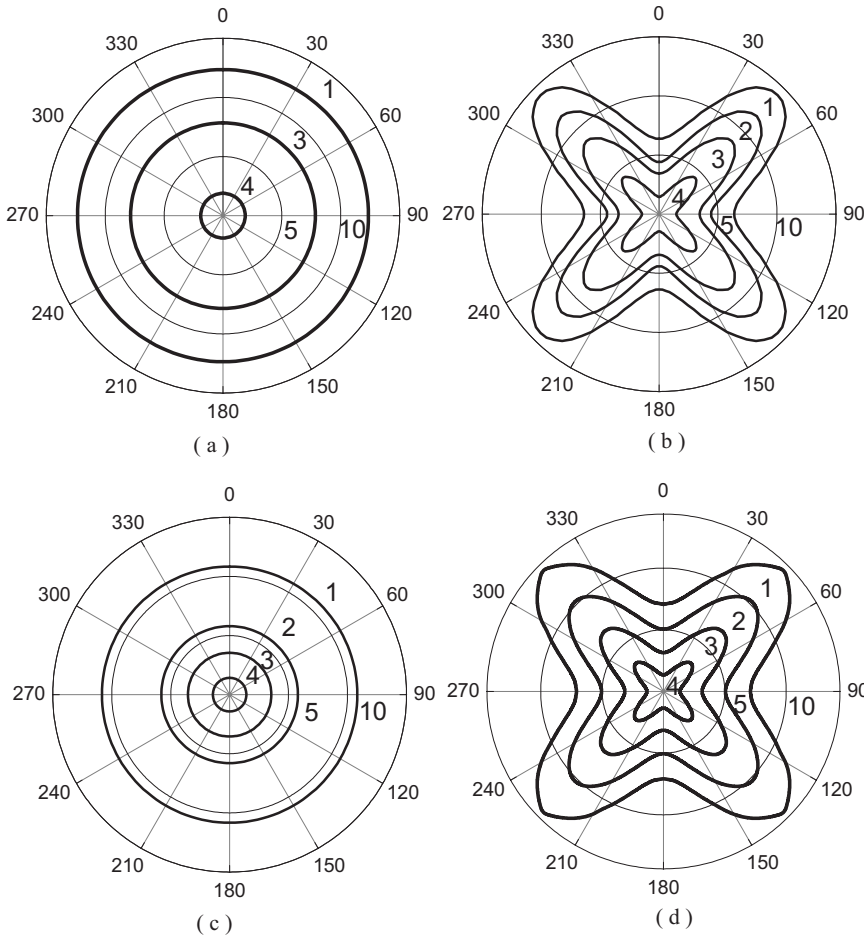


FIG. 14. H_v light scattering patterns at $a/\lambda=1$ calculated by using Eqs. (17)–(31) as a function of b/a and length-to-width x : (a) $b/a=1$ for $x=3$; (b) $b/a=1.5$ for $x=3$; (c) $b/a=1$ for $x=7$; (d) $b/a=1.5$ for $x=7$. The intensity magnitude signals are represented as four counter curves: (1) 1.0×10^{-2} ; (2) 1.2×10^{-2} ; (3) 1.3×10^{-2} ; (4) 1.4×10^{-2} .

$$I_{H_v} = \int_0^\pi \int_0^\infty \{f(r) \left(-\frac{1}{960}(5 \cos^4 \alpha + 30 \cos^2 \alpha - 27) + \frac{1}{192} \cos^2 \frac{\theta}{2} (5 \cos^4 \alpha + 6 \cos^2 \alpha - 3) \right) \times \cos[hr \cos \alpha] r^2 \sin \alpha dr d\alpha. \quad (33)$$

By integrating Eq. (33) by α , Eq. (33) becomes

$$I_{H_v} = \int_0^\infty \mu'(r) f(r) \left\{ \left(-\frac{1}{h^4 r^4} + \frac{1}{h^2 r^2} - \frac{1}{15} \right) \frac{\sinh r}{4hr} + \left(\frac{1}{2h^2 r^2} - \frac{1}{3} \right) \frac{\cosh r}{2h^2 r^2} + \cos^2 \frac{\theta}{2} \left[-\frac{1}{64} - \left(\frac{5}{h^4 r^4} + \frac{3}{h^2 r^2} - \frac{11}{24} \right) \frac{\sinh r}{4hr} - \left(\frac{5}{4h^2 r^2} - \frac{1}{3} \right) \frac{\cosh r}{h^2 r^2} \right] \right\} r^2 dr. \quad (34)$$

Equation (34) [or Eq. (33)] indicates no μ -dependence of a scattering lobe showing a circular pattern, but it is different from the formula of scattered intensity derived by Stein *et al.* [40] and Matsuo *et al.* [35] in the case in which the optical axes correspond to the chain axes.

Figure 14 shows H_v scattering patterns calculated by using Eqs. (23)–(31) at $a/\lambda=1$. The values of parameter b/a were chosen to be 1 and 1.5. The values of the length-to-

width ratio x revealing an ideal axial ratio of a rod were chosen to be 3 and 7. The calculated patterns showed the sensitive μ -dependence to b/a , while the patterns were hardly affected by the value of x . This means that the orientation function $\omega(\theta)[f_T(\Psi)]$ shown in Fig. 12 does not influence the H_v patterns strongly. This is different from the patterns calculated by spherulite [41] and rod [42] models, in which the optical axes fixed with respect to a rod axis and a radial axis provide clear μ -dependent lobes rather than those with orientation fluctuation. Furthermore, the patterns show a somewhat circular type at $b/a=1$ with the same profile of the correlation functions of $f(r)$ and $g(r)$.

Judging from the observed patterns in Fig. 10, the correlation distance for the azimuthal (rotational) angle ϕ_{ij} becomes stronger with elapsing annealing time. Such an interesting phenomenon gave the same tendency as the patterns calculated by setting the optical axis to be the chain axis [34]. This indicates that the correlation distance of $g(r)$ is more effective in providing clear μ -dependent patterns than the correlation distance of $f(r)$.

In conclusion, the density fluctuation by chain diffusion was induced when the trans-fraction, indicating the rigidity of an amorphous PET chain, increased beyond a critical content. Beyond this critical content, chain ordering was accelerated by the progression of the density fluctuation, and initial crystallization occurred in the polymer denser highly ordered regions.

IV. CONCLUSION

The driving force of density fluctuation of amorphous PET films under the annealing processes was analyzed synthetically by using depolarized light scattering, SAXS, WAXD, and FTIR. The analysis was performed on the basis of logarithmic light scattered intensity $\ell n(I)$ versus annealing time. The relationship was classified into three stages: the first stage (stage I), where $\ell n(I)$ showed barely any change with time; the second stage (stage II), where $\ell n(I)$ increased linearly; and the third stage (stage III), where the intensity deviated from the linear relationship and essentially reached a static value. The increment of trans-fraction in an amorphous chain provided chain diffusion to pursue molecular ordering by the chain coagulation. Namely, it was concluded that the density fluctuation termed “quasi-spinodal decomposition” in stage II was closely related to the conversion from a gauche- to a trans-conformation. Here, the density fluctuation by chain diffusion occurred when the trans-fraction reached a critical content and the resultant amorphous chain rich regions by density fluctuation provided the initiation of crystallization (stage III). In stage I associated with the conversion, no increase in density occurred, but the storage modulus of the film increased with annealing time. This indicated that an increase in the trans-fraction influenced an

increase in Young’s modulus without increasing the bulk density. The lattice model supported the concept that an increase of the trans-fraction accelerated the preferred orientation of rods corresponding to rigid chain segments with respect to the direction connected between the cross-link points. The theoretical orientation distribution functions were characterized by a relatively large length-to-width ratio x associated with an increase in the trans-fraction, indicating that the orientation distribution function became sharper with increasing chain rigidity. By using the orientation function, the H_v light scattering patterns were calculated by a statistical approach. Here, the optical axis of a PET chain segment was chosen perpendicular to the chain direction and the benzene ring on the basis of refractive indices of a PET segment. In the model system, two correlation fluctuations concerning correlated orientation fluctuation and correlated rotational fluctuations between the optical elements were introduced as exponential types represented by their correlation distance. The calculated patterns provided a clear X-type lobe when the correlation concerning the rotational fluctuation became stronger. The calculated patterns were in good agreement with the patterns observed in stage III. This indicated that the PET chains in the amorphous film became less active as the annealing time elapsed in stage III. This was due to the initiation of crystallization.

-
- [1] M. Imai, K. Kaji, and T. Kanaya, *Phys. Rev. Lett.* **71**, 4162 (1993).
- [2] M. Imai, K. Kaji, T. Kanaya, and Y. Sakai, *Phys. Rev. B* **52**, 12696 (1995).
- [3] J. Radhakrishnan and A. Kaito, *Polymer* **42**, 3859 (2001).
- [4] M. Imai, K. Mori, T. Mizukami, K. Kaji, and T. Kanaya, *Polymer* **33**, 4451 (1992).
- [5] J.-M. Huang, P. P. Chu, and F.-C. Chang, *Polymer* **41**, 1741 (2000).
- [6] M. Imai, K. Kaji, and T. Kanaya, *Macromolecules* **27**, 7103 (1994).
- [7] G. le Bourvellec, L. Monnerie, and J. P. Jarry, *Polymer* **28**, 1712 (1987).
- [8] T. Xu, Y. Z. Bin, Y. Nakagaki, and M. Matsuo, *Macromolecules* **37**, 6985 (2004).
- [9] T. Xu, Y. Bin, N. Djourelou, T. Suzuki, and M. Matsuo, *Phys. Rev. B* **71**, 075204 (2005).
- [10] R. Rastogi, W. P. Vellinga, S. Rastogi, C. Shick, and H. E. H. Meijer, *J. Polym. Sci., Part B: Polym. Phys.* **42**, 2092 (2004).
- [11] H. Morita, T. Kawakatsu, and M. Doi, *Macromolecules* **34**, 8777 (2001).
- [12] B. Erman, I. Bahar, A. Kloczkowski, and J. E. Mark, *Macromolecules* **23**, 5335 (1990).
- [13] I. Bahar, B. Erman, A. Kloczkowski, and J. E. Mark, *Macromolecules* **23**, 5341 (1990).
- [14] G. H. Meeten and P. Navard, *J. Polym. Sci., Polym. Phys. Ed.* **22**, 2159 (1984).
- [15] G. H. Meeten and P. Navard, *J. Polym. Sci., Part B: Polym. Phys.* **26**, 413 (1988).
- [16] Y. G. Zhu, Z. Q. Li, D. Zhang, and T. Tanimoto, *J. Polym. Sci., Part B: Polym. Phys.* **44**, 1351 (2006).
- [17] N. J. Terrill, P. A. Fairclough, E. Towns-Andrews, B. U. Komschek, R. J. Young, and A. J. Ryan, *Polymer* **39**, 2381 (1998).
- [18] H. Furukawa, *Adv. Phys.* **34**, 703 (1985).
- [19] J. W. Cahn and J. E. Hilliard, *J. Chem. Phys.* **28**, 258 (1958).
- [20] J. W. Cahn, *J. Chem. Phys.* **42**, 93 (1965).
- [21] Y. Zhang, Y. Lu, Y. Duan, J. Zhang, S. Yan, and D. Shen, *J. Polym. Sci., Part B: Polym. Phys.* **42**, 4440 (2004).
- [22] A. C. Middleton, R. A. Duckett, I. M. Ward, A. Mahendrasingam, and C. Martin, *J. Appl. Polym. Sci.* **79**, 1825 (2001).
- [23] K. C. Cole, A. Ajji, and E. Pellerin, *Macromolecules* **35**, 770 (2002).
- [24] C. Pellerin, M. Pérolet, and P. R. Griffiths, *Macromolecules* **39**, 6546 (2006).
- [25] S. K. Bahl, D. D. Cornell, F. J. Boerio, and G. E. McGraw, *J. Polym. Sci., Polym. Lett. Ed.* **12**, 13 (1974).
- [26] F. J. Boerio, S. K. Bahl, and G. E. McGraw, *J. Polym. Sci., Polym. Phys. Ed.* **14**, 1029 (1976).
- [27] Y. Wang, D. Shen, and R. Qian, *J. Polym. Sci., Part B: Polym. Phys.* **36**, 783 (1998).
- [28] R. Qian, D. Shen, and F. Sun, *Macromol. Chem. Phys.* **197**, 1485 (1996).
- [29] Y. Zhang, J. Zhang, Y. Lu, Y. Duan, S. Yan, and D. Shen, *Macromolecules* **37**, 2532 (2004).
- [30] M. Matsuo, J. Ooki, Y. Harashina, T. Ogita, and R. S. Manley, *Macromolecules* **28**, 4951 (1995).
- [31] Y. Bin, A. Koganemaru, T. Nakashima, and M. Matsuo, *Polym. J. (Tokyo, Jpn.)* **37**, 192 (2005).
- [32] M. Matsuo, S. Miyoshi, M. Azuma, Y. Bin, Y. Agari, Y. Sato,

- and A. Kondo, *Macromolecules* **38**, 6688 (2005).
- [33] P. J. Flory, D. Y. Yoon, and K. A. Dill, *Macromolecules* **17**, 862 (1984).
- [34] P. J. Flory and G. Ronca, *Mol. Cryst. Liq. Cryst.* **54**, 289 (1979).
- [35] M. Matsuo, S. Miyoshi, M. Azuma, Y. Nakano, and Y. Bin, *Phys. Rev. E* **72**, 041403 (2005).
- [36] R. Daubeny, C. W. Bunn, and C. Brown, *Proc. R. Soc. London, Ser. A* **226**, 531 (1954).
- [37] C. W. Bunn and R. Daubeny, *Trans. Faraday Soc.* **50**, 1173 (1954).
- [38] N. Sakaguchi, T. Oda, A. Nakai, and H. Kawai, *Sen'i Gakkai-shi* **33**, 779 (1977).
- [39] M. Matsuo, M. Tamada, T. Terada, C. Sawatari, and M. Niwa, *Macromolecules* **15**, 988 (1982).
- [40] R. S. Stein and P. R. Wilson, *J. Appl. Phys.* **33**, 1914 (1962).
- [41] M. Matsuo, K. Geshi, A. Moriyama, and C. Sawatari, *Macromolecules* **15**, 193 (1982).
- [42] M. Matsuo, Y. Sugiura, T. Kimura, and T. Ogita, *Macromolecules* **35**, 4493 (2002).